Available online at www.sciencedirect.com
ScienceDirect
International Journal of Heat and Mass Transfer 50 (2007) 2952–2968
International Journal of HEAT and MASS TRANSFER
www.elsevier.com/locate/ijhmt

Multiscale modeling of particle–solidification front dynamics, Part I: Methodology

J.W. Garvin, Y. Yang, H.S. Udaykumar *

Department of Mechanical and Industrial Engineering, The University of Iowa, Iowa City, IA 52242, United States

Received 19 February 2006; received in revised form 14 December 2006
Available online 21 March 2007

Abstract

The interaction between an advancing solidification front and a micron-size particle is an inherently multiscale heat and mass transport problem. Transport at the micro-scale (i.e. the scale of the particle dimension) couples with intermolecular interactions and lubrication forces in a thin layer of melt between the particle and the front to determine the overall dynamics of the interaction. A multiscale model is developed to simulate such front–particle interactions. The solution to the lubrication equations in the melt layer is coupled to the solution of the Navier–Stokes equations for the overall particle–front system. Techniques are developed for coupling the dynamics at the two disparate scales at a common "matching plane". All interfaces are represented and tracked using the level-set approach. A sharp-interface technique is employed for solution of the governing equations in the resulting moving boundary problem. Validation of the coupling strategy and results for the particle–front interaction phenomenon with the multiscale approach are presented.

1. Introduction

Particle–solidification interactions are crucial in the development of the final microstructure in metal-matrix composites (MMCs). In MMCs, embedded particles (typically ceramics) are introduced in the metallic melt to serve as reinforcements in the final solidified sample. Particle sizes of interest are typically in the micron to millimeter range and are commensurate with the length scales of typical dendritic/cellular crystalline morphologies. Understanding the particle–front interaction phenomenon is important for effecting better control of the distribution of particles in MMCs. As illustrated in Fig. 1, when a solidification front approaches the particle to nanometer-scale separations repulsive disjoining pressures in the intervening melt film become large and cause the particle to move. The motion of the particle draws melt into the gap resulting in a fluid dynamic drag force acting on the particle that impedes its motion [1]. The balance between the drag force and the disjoining pressure force determines the overall dynamics of the particle, i.e. whether the particle will be pushed or engulfed by the advancing front. In general, pushing of the particle by the front is undesirable and may lead to particle depletion/accumulation in specific regions of the solidified material.

An overview of the different models for the drag and intermolecular forces on the particle is given in Asthana et al. [2,3]. Much of the work to date on particle–solidification front interactions relies on simplified analytical expressions for the drag and the repulsive intermolecular force [4–15]. The intermolecular forces are typically modeled as dispersive (van der Waals) interactions [16]. The most common form for the drag force was originally derived [14] for a flat solidification front. However, a flat solidification front can only be achieved in the restricted case of a directional solidification experiment when the thermal conductivity of the particle (k_p) is the same as that of the melt (k_l). Shangguan et al. [7] modified the expressions for the drag and the repulsive force to account for the

* Corresponding author. Tel.: +1 319 384 0832; fax: +1 319 335 5669.
E-mail address: ush@icaen.uiowa.edu (H.S. Udaykumar).

0017-9310/$ - see front matter © 2007 Elsevier Ltd. All rights reserved.
doi:10.1016/j.ijheatmasstransfer.2006.12.031

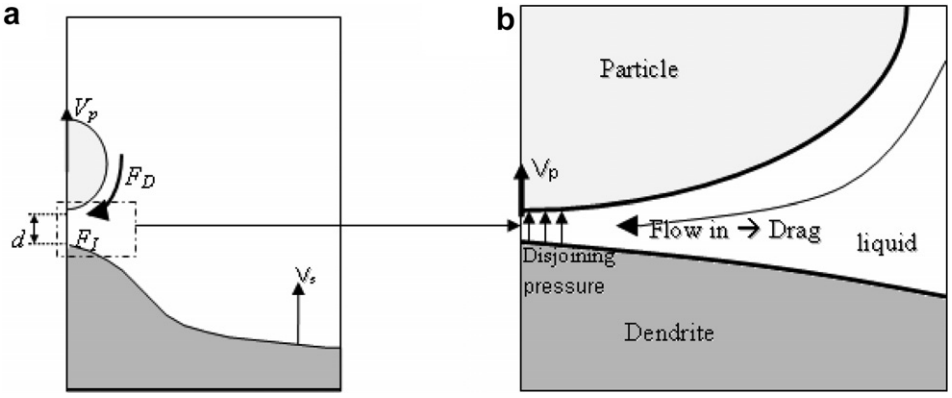

Fig. 1. (a) Schematic of the overall system. (b) Schematic of the zoomed-in box in (a) illustrating the different mechanisms involved in the particle–solidification front interaction. As the solidification front approaches the particle, the disjoining pressure (for the repulsive van der Waals interaction between the surfaces) starts to push the particle. Fluid then flows in to replenish the gap which results in a drag force F_D that opposes the intermolecular force F_I.

non-planarity of the solidification front when the thermal conductivity of the particle is different from the melt [1,12]. A large portion of the theoretical research on front–particle interactions has employed steady-state analyses under the condition where the particle is being steadily pushed by the front [5,7,8,10,14,17]. Dynamic models that simulate the interaction and subsequent evolution of an initially stationary particle being approached by a front have been developed in recent work [11,12,15]. However, in all these papers (including previous papers by the present authors [11–13]) semi-empirical models were used for the interaction forces.

The present work seeks to remove all of the restrictions placed in previous work by developing a dynamic, fully-coupled particle–front interaction model that accounts for non-planarity of the front and the multiscale nature of the problem. In this first paper the computational technique for performing such coupled multiscale calculations is developed. The novel aspect in this work is the use of a sharp-interface, fixed grid methodology with levelsets for interface representation. The computational domain is split into regions where distinct physical phenomena at disparate length and time scales occur. Procedures are developed to couple these phenomena at a matching plane. This approach represents a departure from previous work [11–13] and results in a generally applicable computational methodology for coupling phenomena at different scales. There is no need for semi-empirical force models in the present framework. No restrictions on planarity of the front are placed. The companion paper (hereinafter referred to as Part II) will present results obtained for particle–solidification interactions using the model as well as provide a thorough discussion of the physics involved. In Part II it is shown that the technique presented herein yields insights into the physics underlying the particle–front interaction viewed as the evolution of the particle–front dynamical system and removes the limitations inherent in the previous quasi-static equilibrium viewpoint [11–15].

2. Development of the multiscale model

2.1. Overall approach

The computational method used for the outer microscale calculations was developed in Marella et al. [18] and Yang et al. [19] for simulation of flows around moving boundaries. In this study, there are two moving boundaries present in the domain. The solid–liquid phase boundary (denoted by subscript s-l) advances under the applied boundary conditions. The particle (denoted by subscript p) moves under the influence of the interaction forces with the phase front. All interfaces are represented implicitly on the mesh using a standard level-set approach [20–23] which is widely used to represent and track interfaces [24,25]. The level-set method advects a scalar field ϕ in addition to the flow variables. The value of ϕ at any point is its signed normal distance from the interface with $\phi < 0$ inside the immersed boundaries and $\phi > 0$ outside. The interface location is implicitly embedded in the ϕ-field since $\phi = 0$ contours represent the immersed boundary. In this work the notation $\phi_a(\vec{X}_b, t)$ will be used. Subscript "a" indicates the level-set corresponding to the interface a (=p/s-l) located at the point "b". The t denotes time and $\vec{X}_b$ indicates the position vector of point "b". The geometry is communicated to the flow solver solely through the distance function field. The sharp-interface embedded boundary treatment uses an appropriate modification of the stencil for the mesh points adjoining the boundaries. This does not smear discontinuities at the interface and does not require forcing terms to transmit boundary effects to the fluid. The discretization depends essentially on convolving the differential operators with the distance function field inherent in the level-set representation of the interfaces. The result is an easily implemented algorithm where the discretization of the governing equations at all points (i.e. away from as well as adjoining the interface) can be presented in a unified format [18,19,26].

A schematic of the configuration under study is shown in Fig. 2. The overall computational domain is partitioned into two regions corresponding to the two disparate scales that are relevant to the problem. The two scales of concern are termed "inner" (melt gap) and "outer" (front–particle system) scales. In the outer (micro-) scale the Navier–Stokes equations are solved. However, solving the Navier–Stokes equations in the thin gap between the solidification front and the particle would require an impossibly fine mesh. Therefore an embedded inner model is developed by solving a lubrication equation in the gap (Fig. 2b). The solution from the lubrication equation is then coupled with the outer Navier–Stokes solution at a "matching plane" (see Fig. 2b). This coupling between the two scales is maintained throughout the process of front approach to the particle and the subsequent dynamics leading to particle pushing or engulfment by the front. In the following sections, the equations for the outer and the inner regions and the method for matching the solutions are described.

2.2. The governing equations in the "outer region"

The outer region is defined by removing the thin melt gap region from the overall computational domain shown in Fig. 2. The outer variables are non-dimensionalized as follows:

$$T^* = \frac{T - T_m}{T_c}, \quad x^* = \frac{x}{R_p}, \quad y^* = \frac{y}{R_p}, \quad p^*_{outer} = \frac{p}{p_{Couter}},$$
$$u^* = \frac{u}{U_c}, \quad v^* = \frac{v}{U_c}, \quad t^* = \frac{t}{t_c}$$

Here T is temperature, x and y are the outer coordinates, p is the pressure, t is time, and u and v are the x- and y-fluid velocities, respectively. The "*" superscripts denote the non-dimensional variables and the "c" subscripts denote the characteristic scales. The characteristic scales are defined as follows: $U_c = \alpha_l/R_p$, $T_c = G_L R_p$, $t_c = R_p/U_c$, and $p_{Couter} = \rho U_c^2$. The characteristic pressure is denoted as p_{Couter} to distinguish it from the inner characteristic pressure scale (p_{Cinner}), which will be defined later in the text.

The T_m and the R_p denote the melting temperature of the melt and the particle radius, respectively. The ρ and α_l denote the density and thermal diffusivity of the melt, respectively, and G_L is the temperature gradient imposed in the liquid during the simulations.

The non-dimensional governing equations are:

Continuity:

$$\frac{\partial u^*}{\partial x^*} + \frac{\partial v^*}{\partial y^*} = 0 \tag{1a}$$

x-momentum:

$$\frac{\partial u^*}{\partial t^*} + u^*\frac{\partial u^*}{\partial x^*} + v^*\frac{\partial u^*}{\partial y^*} = -\frac{1}{\rho}\frac{\partial p^*_{outer}}{\partial x^*} + \frac{1}{Re}\left(\frac{\partial^2 u^*}{\partial x^{*2}} + \frac{\partial^2 u^*}{\partial y^{*2}}\right) \tag{1b}$$

y-momentum:

$$\frac{\partial v^*}{\partial t^*} + u^*\frac{\partial v^*}{\partial x^*} + v^*\frac{\partial v^*}{\partial y^*} = -\frac{1}{\rho}\frac{\partial p^*_{outer}}{\partial y^*} + \frac{1}{Re}\left(\frac{\partial^2 v^*}{\partial x^{*2}} + \frac{\partial^2 v^*}{\partial y^{*2}}\right) \tag{1c}$$

Energy:

$$\frac{\partial T^*}{\partial t^*} + u^*\frac{\partial T^*}{\partial x^*} + v^*\frac{\partial T^*}{\partial y^*} = \alpha^*_{s/l/p}\left(\frac{\partial^2 T^*}{\partial x^{*2}} + \frac{\partial^2 T^*}{\partial y^{*2}}\right) \tag{1d}$$

where $Re = \frac{\rho U_c R_p}{\mu}$ is the Reynolds number, μ denotes the dynamic viscosity of the liquid, and $\alpha^*_{s/l/p} = \frac{\alpha_{s/l/p}}{\alpha_l}$ is the non-dimensional thermal diffusivity of the solid/liquid/particle phase, respectively.

The no-slip and no-penetration boundary conditions are applied at the particle surface, i.e.:

$$\vec{v}^*(\vec{X}^*_p, t^*) = \vec{v}^*_p \tag{2}$$

where $\vec{v}^*(\vec{X}^*_p, t^*)$ is the fluid velocity vector at time t^* and position $\vec{X}^*_p$ (position vector at the particle surface), and $\vec{v}^*_p$ is the particle velocity. Ignoring shrinkage effects upon solidification, the velocity boundary condition at the phase boundary (solidification front) is:

$$\vec{v}^*(\vec{X}^*_{s\text{-}l}, t^*) = \vec{v}^*_{s\text{-}l} = 0 \tag{3}$$

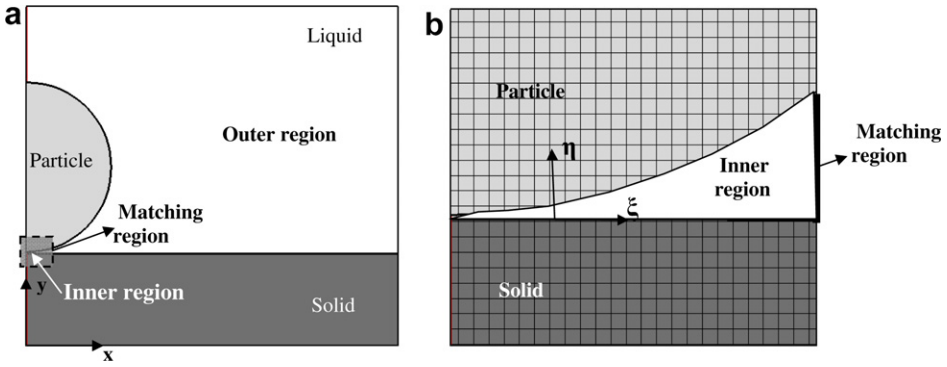

Fig. 2. (a) Schematic of a solidification front moving towards and interacting with a particle. (b) A zoomed in view of the solidification front in (a) interacting with the particle. The rectangular grid in (b) represents the mesh. The bold line on the right denotes the "matching plane".

The solidification front velocity is computed from the Stefan condition:

$$s^*_{s\text{-}l} = Ste\left(\left(\frac{k_s}{k_l}\right)\left(\frac{\partial T^*}{\partial n^*}\right)_s - \left(\frac{\partial T^*}{\partial n^*}\right)_l\right) \tag{4}$$

where $s^*_{s\text{-}l}$ is the non-dimensional interface speed in the direction normal to the interface, k_s is the thermal conductivity of the solid and $\mathrm{Ste} = k_l G_L/(\rho H_{sl} U_c)$ is the Stefan number. H_{sl} is the latent heat of fusion per unit mass of the melt. Note that $v^*_{s\text{-}l}$ is fluid velocity at the solidification front whereas $s^*_{s\text{-}l}$ is the speed at which the solidification front is traveling.

The solidification front temperature is assumed to be at the melting temperature (i.e. $T_{s\text{-}l} = T_m$) or depressed due to premelting effects [8,13,27] and is given by:

$$T^*_{s\text{-}l} = -\left(\frac{\lambda}{d_c d^*}\right)^3\left(\frac{T_m}{G_L R_p}\right) \tag{5}$$

In the above the non-dimensional gap thickness between the solidification front and the particle is given by d^*. The characteristic value of the gap thickness is given by d_c (=$0.15R_p$). The variable, λ, is a length-scale corresponding to molecular interactions whose value is typically around 10^{-10} m [8]. For sufficiently large values of gap thickness the interface temperature is essentially the equilibrium melting temperature, while a depression of melting temperature results as the front approaches the particle and a premelted layer of melt is formed between the two surfaces [27]. In the current work curvature effects on interfacial temperature (through the Gibbs–Thompson condition) are neglected. These effects, for the micron size particle considered, are likely to have a significant effect, and can be included fairly easily in the computations [19,28]. However, past theoretical work on particle–front interaction has largely ignored this effect and this practice is followed herein to isolate the effects of thermal transport and flow. In ongoing work, the effect of interfacial temperature change due to curvature is being studied.

At the interface between the particle and the melt heat flux balance:

$$\left(\frac{k_p}{k_l}\right)\left(\frac{\partial T^*}{\partial n^*}\right)_p = \left(\frac{\partial T^*}{\partial n^*}\right)_l \tag{6}$$

The normal gradients of temperature in Eqs. (4) and (6) are computed using the normal probe technique described in previous work [19].

2.3. Modeling the "inner region" using lubrication theory

2.3.1. Equations for the "inner region"

The inner region is defined by the melt gap between the front and the particle that is excised from the overall computational domain. In this region, viscous and repulsive intermolecular forces dominate and a lubrication layer assumption is applied. To include the repulsive intermolecular interactions, a model for disjoining pressure in the thin film is included in the lubrication model [16,29]. A typical form of the disjoining pressure (Π) is given by:

$$\Pi = \frac{A}{6\pi d^3} \tag{7}$$

where A is the Hamaker constant (which is typically of the order of $\pm 10^{-19}$ J) and d is the gap thickness between the two surfaces (in the present case, the particle and solidification front).

To develop the inner lubrication model the governing equations are transformed into local curvilinear (ξ, η) coordinates as illustrated in Fig. 2. The resulting transformed equations are as follows [30]. The continuity equation is:

$$\frac{\partial U}{\partial \xi} + \frac{\partial V}{\partial \eta} = 0 \tag{8}$$

where:

$$U = u y_\eta - v x_\eta \tag{9}$$

$$V = v x_\xi - u y_\xi \tag{10}$$

The momentum equations are:

$$\begin{aligned}&\frac{\partial(J\rho u)}{\partial t} + \frac{\partial(\rho U u)}{\partial \xi} + \frac{\partial(\rho V u)}{\partial \eta}\\ &\quad = -\left\{\frac{\partial y}{\partial \eta}\frac{\partial p}{\partial \xi} - \frac{\partial y}{\partial \xi}\frac{\partial p}{\partial \eta}\right\} + \frac{\partial}{\partial \xi}\left[\frac{\mu}{J}\left(q_1\frac{\partial u}{\partial \xi} - q_2\frac{\partial u}{\partial \eta}\right)\right]\\ &\qquad + \frac{\partial}{\partial \eta}\left[\frac{\mu}{J}\left(q_3\frac{\partial u}{\partial \eta} - q_2\frac{\partial u}{\partial \xi}\right)\right] - \left\{\frac{\partial y}{\partial \eta}\frac{\partial \Pi}{\partial \xi} - \frac{\partial y}{\partial \xi}\frac{\partial \Pi}{\partial \eta}\right\}\end{aligned} \tag{11}$$

$$\begin{aligned}&\frac{\partial(J\rho v)}{\partial t} + \frac{\partial(\rho U v)}{\partial \xi} + \frac{\partial(\rho V v)}{\partial \eta}\\ &\quad = -\left\{\frac{\partial x}{\partial \xi}\frac{\partial p}{\partial \eta} - \frac{\partial x}{\partial \eta}\frac{\partial p}{\partial \xi}\right\} + \frac{\partial}{\partial \xi}\left[\frac{\mu}{J}\left(q_1\frac{\partial v}{\partial \xi} - q_2\frac{\partial v}{\partial \eta}\right)\right]\\ &\qquad + \frac{\partial}{\partial \eta}\left[\frac{\mu}{J}\left(q_3\frac{\partial v}{\partial \eta} - q_2\frac{\partial v}{\partial \xi}\right)\right] - \left\{\frac{\partial x}{\partial \xi}\frac{\partial \Pi}{\partial \eta} - \frac{\partial x}{\partial \eta}\frac{\partial \Pi}{\partial \xi}\right\}\end{aligned} \tag{12}$$

The energy equation is:

$$\begin{aligned}&\frac{\partial(Jc_p\rho T)}{\partial t} + \frac{\partial(\rho c_p U T)}{\partial \xi} + \frac{\partial(\rho c_p V T)}{\partial \eta}\\ &\quad = \frac{\partial}{\partial \xi}\left[\frac{k_l}{J}\left(q_1\frac{\partial T}{\partial \xi} - q_2\frac{\partial T}{\partial \eta}\right)\right]\\ &\qquad + \frac{\partial}{\partial \eta}\left[\frac{k_l}{J}\left(q_3\frac{\partial T}{\partial \eta} - q_2\frac{\partial T}{\partial \xi}\right)\right]\end{aligned} \tag{13}$$

J is the standard Jacobian of the metric tensor and q_1, q_2, q_3 are metrics of the transformation [31]. The ξ and η subscripts denote differentiation with respect to that independent variable. c_p is the specific heat of the melt.

To develop the lubrication equations the thin layer assumption for the melt gap is made, i.e. the gap thickness $\max(d(\xi)) \ll R_p$ (the outer length scale). The inner variables are then non-dimensionalized with respect to the scales applicable in the lubrication layer as follows:

$$T^* = \frac{T}{T_c}, \quad J^* = \frac{J}{J_c}, \quad x^* = \frac{x}{R_p}, \quad y^* = \frac{y}{R_p}, \quad q_1^* = \frac{q_1}{q_{1c}},$$
$$q_3^* = \frac{q_3}{q_{3c}}, \quad p_{inner}^* = \frac{p}{p_{Cinner}}, \quad \Pi^* = \frac{\Pi}{p_{Cinner}}, \quad \xi^* = \frac{\xi}{R_p},$$
$$\eta^* = \frac{\eta}{d_c}, \quad U^* = \frac{U}{U_c}, \quad u^* = \frac{u}{U_c}, \quad v^* = \frac{v}{V_c}, \quad t^* = \frac{t}{t_c}$$

where the "*" superscripts denote the non-dimensional variables and the "c" subscripts denote the characteristic scales. The characteristic inner pressure is given by: $p_{Cinner} = R_p^2 \mu U_c/(d_c^3)$.

The continuity equation (Eq. (8)) gives a relation between the two characteristic velocities, U_c and V_c:

$$V_c = \left(\frac{d_c}{R_p}\right) U_c \tag{14}$$

Combining Eqs. (8)–(13), and applying the lubrication layer assumption leads to:

$$\frac{\partial U^*}{\partial \xi^*} + \frac{\partial V^*}{\partial \eta^*} = 0 \tag{15}$$

$$-\left(\frac{(J_O^*)^3}{J_{NO}^* q_3^*}\right)\left(\frac{\partial p_{inner}^*}{\partial \xi^*} + \frac{\partial \Pi^*}{\partial \xi^*}\right) + \frac{\partial^2 U^*}{\partial \eta^{*2}} = 0 \tag{16}$$

$$\left(\frac{\partial p_{inner}^*}{\partial \eta^*} + \frac{\partial \Pi^*}{\partial \eta^*}\right) = 0 \tag{17}$$

$$\frac{\partial^2 T^*}{\partial \eta^{*2}} = 0 \tag{18}$$

where:

$$J_{NO}^* = x_\xi^* y_\eta^* - x_\eta^* y_\xi^* \tag{19}$$

and

$$J_O^* = \sqrt{q_1^* q_3^*} \tag{20}$$

From Eq. (17), as expected in the lubrication approximation the pressure and the disjoining pressure are functions of ξ only. This allows one to integrate Eq. (16) to obtain:

$$U^* = \frac{1}{2}\left[\left(\frac{(J^*)^3}{J_{NO}^* q_3^*}\right)\left(\frac{\partial p_{inner}^*}{\partial \xi^*} + \frac{\partial \Pi^*}{\partial \xi^*}\right)\right]\eta^{*2} + C_1\eta^* + C_2 \tag{21}$$

The boundary conditions at the solid–liquid interface and the particle surface are:

$$U^*(\eta^* = 0) = U_{s\text{-}l}^*; \quad V^*(\eta^* = 0) = V_{s\text{-}l}^* \tag{22a}$$
$$U^*(\eta^* = d^*) = U_p^*; \quad V^*(\eta^* = d^*) = V_p^* \tag{22b}$$

where d^* is the non-dimensional gap thickness, which is a function of ξ^*. The U_p^*, $U_{s\text{-}l}^*$, V_p^*, and $V_{s\text{-}l}^*$ are the velocity components for the particle (subscript p and solidification front (subscript s-l) found from Eqs. (9) and (10) and are defined as:

$$U_p^* = u_p^* y_\eta - v_p^* x_\eta; \quad U_{s\text{-}l}^* = 0 \tag{23a}$$
$$V_p^* = v_p^* x_\xi - u_p^* y_\xi; \quad V_{s\text{-}l}^* = 0 \tag{23b}$$

Applying the boundary conditions given in Eqs. (22) to (21) yields:

$$U^* = \frac{1}{2}\left[\left(\frac{(J^*)^3}{J_{NO}^* q_3^*}\right)\left(\frac{\partial p_{inner}^*}{\partial \xi^*} + \frac{\partial \Pi^*}{\partial \xi^*}\right)\right](\eta^{*2} - d^*\eta^*) + \left(\frac{U_p^* - U_{s\text{-}l}^*}{d^*}\right)\eta^* \tag{24}$$

Substituting U^* from Eq. (24) into Eq. (15) and integrating across the gap gives:

$$\int_0^{d^*} \frac{\partial U^*}{\partial \xi^*} d\eta^* + V_p^* - V_{s\text{-}l}^* = 0 \tag{25}$$

Substituting Eq. (24) into Eq. (25) yields the equation for pressure in the gap:

$$-\left(\frac{(J^*)^3}{J_{NO}^* q_3^*}\right)\left[\left(\frac{\partial^2 p_{inner}^*}{\partial \xi^{*2}} + \frac{\partial^2 \Pi^*}{\partial \xi^{*2}}\right)\frac{d^{*3}}{12} + \left(\frac{\partial p_{inner}^*}{\partial \xi^*} + \frac{\partial \Pi^*}{\partial \xi^*}\right)\frac{\partial d^*}{\partial \xi^*}\left(\frac{d^{*2}}{4}\right)\right] + \frac{1}{2}\left(d^* \frac{\partial\left(U_p^* - U_{s\text{-}l}^*\right)}{\partial \xi^*} + (U_p^* - U_{s\text{-}l}^*) d^{*2} \frac{\partial}{\partial \xi^*}\left(\frac{1}{d^*}\right)\right) + V_p^* - V_{s\text{-}l}^* = 0 \tag{26}$$

It is easily checked that this equation reduces to the standard Reynolds' equation in lubrication theory [29,32] for a Cartesian coordinate system. Eq. (26) is solved for the pressure in the gap (p_{inner}^*) between the particle and the solidification front. Note, as suggested by Eq. (23), that the fluid velocity at the solidification front is zero (i.e. $V_{s\text{-}l}^* = U_{s\text{-}l}^* = 0$) unless one includes shrinkage effects. In this paper it is assumed that there is no shrinkage-induced flow. In most situations the particle velocity in the ξ^*-direction can also be considered negligible, however it is retained in Eq. (26) for the sake of generality.

2.3.2. Discretization and mesh-refinement for the "inner region"

2.3.2.1. Defining the inner region. Since a lubrication layer assumption is made for the melt gap, its geometry is defined by means of a gap thickness distribution $d(\xi)$ where ξ is the curvilinear coordinate along the solid–liquid interface, as shown in Fig. 2b. The procedure for finding $d(\xi)$ begins by spanning over the grid points that lie immediately within the particle surface (see [18,19] for details on identification of such "interfacial" points), as shown in Fig. 3. At each of these points (subscripted cp) the corresponding location on the particle surface can be found via:

$$X_p = X_{cp} - \phi_p n_{x_{cp}} \tag{27}$$
$$Y_p = Y_{cp} - \phi_p n_{y_{cp}} \tag{28}$$

where X_p and Y_p are the x- and y-locations, respectively, on the particle surface (or in vector form, $\vec{X}_p$). The $n_{x_{cp}}$ and $n_{y_{cp}}$ are the x- and y-components of the normal (defined as positive pointing away from the particle surface). The ϕ_p, as defined in Section 2.1, is the distance function value for the particle at the points denoted as cp.

For each point on the particle surface denoted by the subscript p above, the corresponding location of a point

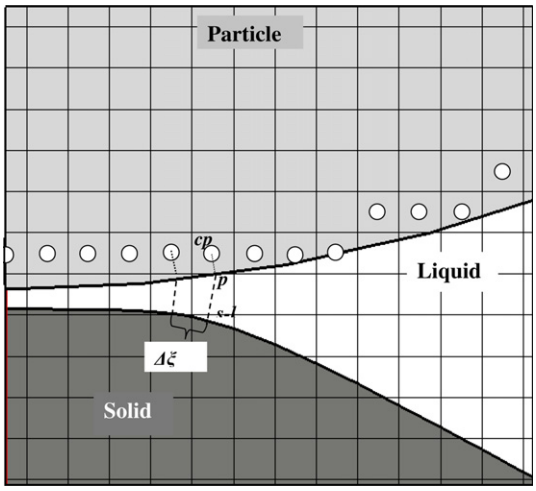

Fig. 3. Illustration of the method for finding the d-distribution. The "i" subscripts indicate the mesh index number.

along the normal (of the solidification front) and lying on the solidification front is:

$$X_{\text{s-l}} = X_{\text{p}} - \phi_{\text{s-l}} n_{x_{\text{p}}} \tag{29}$$

$$Y_{\text{s-l}} = Y_{\text{p}} - \phi_{\text{s-l}} n_{y_{\text{p}}} \tag{30}$$

where $X_{\text{s-l}}$ and $Y_{\text{s-l}}$ are the coordinates on the solidification front. The $n_{x_{\text{p}}}$ and $n_{y_{\text{p}}}$ are the respective x- and y-components of the normal of the solidification front obtained at the particle surface (i.e. at X_{p} and Y_{p}), and the $\phi_{\text{s-l}}$ is the distance function value for the solidification front at the particle surface.

The procedure above identifies a set of N points on the particle surface (subscripted p) and their corresponding partner points s-l on the solid–liquid interface. To form a grid in the inner region these points need to be sequenced to lie along the ξ-coordinate with the first point (i.e. point $i = 1$) located on the west symmetry line (i.e. the point where the gap thickness is at a minimum). Generalizing this sequencing procedure for non-symmetric cases requires a more complicated algorithm and is the subject of ongoing work. Thus, the grid spacing $\Delta\xi$ in the discretization of the inner region is defined as the distance between each of the sequenced solidification front location points, i.e:

$$\Delta\xi_i = \sqrt{(X_{\text{s-l},i} - X_{\text{s-l},i+1})^2 + (Y_{\text{s-l},i} - Y_{\text{s-l},i+1})^2} \tag{31}$$

where the subscripts "i" and "$i+1$" indicate the inner mesh indices. The thickness of the gap d_i at a given point in the inner mesh is then obtained for all i from 1 to N as the value $\phi_{\text{s-l}}(\vec{X}_{\text{p}}, t)$, i.e. the distance function value corresponding to the solidification front at the particle location.

2.3.2.2. Refinement of the inner region and convergence criterion for accurate solution of the lubrication equation. The inner lubrication equation is rather stiff due to the dependency of the disjoining pressure forces on d^{-3}. For small values of d steep variations of hydrodynamic and disjoining pressures are expected in the lubrication layer. The initial d^*-distribution and the inner mesh that is found from the level-set field is too coarse to accurately solve for the pressure in the gap using Eq. (26). Therefore the initial mesh for the "inner region" needs to be refined such that the mesh spacing ($\Delta\xi$) is commensurate with the gap thickness (d). To determine how much to refine the inner mesh, a refinement parameter, R_{f}, is introduced and will be used as a scale factor for the mesh spacing. The R_{f} is defined as:

$$R_{\text{f}} = \frac{R_{\text{p}} \Delta x^*}{d_{\text{c}} d^*_{\min}} \tag{32}$$

where Δx^* is the grid size in the outer domain and $d^*_{\min}$ is the minimum (non-dimensional) gap thickness. Since the inner mesh spacing is initially of the order of the outer mesh spacing, the refined inner mesh spacing is obtained as:

$$\Delta\xi^*_{R_{\text{f}}} = \frac{\Delta\xi^*}{R_{\text{f}}} \tag{33}$$

where $\Delta\xi^*_{R_{\text{f}}}$ is the new, refined grid size in the inner region. The inner mesh is then "re-meshed" using the new inner mesh spacing. The values of the input variables in the embedded lubrication model (i.e. $U^*_{\text{s-l}}$, $V^*_{\text{s-l}}$, d^*, etc.) at the new 'refined' grid points are then linearly interpolated from what was obtained initially at the initial (pre-refined) $\Delta\xi^*$ grid points.

This refinement method aids in the convergence and accuracy of the solution of Eq. (26). A standard Gauss–Seidel iteration was used to solve Eq. (26). Various convergence criteria were examined for this solution method and the one found to work best was:

$$\frac{\sqrt{\sum_i^{k_{\max}} \left(p^{*m}_{\text{inner}} - p^{*m-1}_{\text{inner}}\right)^2}}{\frac{\sum_i^{k_{\max}} p^{*m}_{\text{inner}}}{k_{\max}}} \leqslant \varepsilon_{\text{crit}} \tag{34}$$

where $k_{\max}$ is the total number of grid points, the index m denotes the solution iteration number, the index i denotes a particular grid point, and $\varepsilon_{\text{crit}}$ is the convergence criterion. It was found that a $\varepsilon_{\text{crit}}$ of 10^{-3} was sufficient for all calculations performed.

2.4. Coupling between the inner and outer regions at the matching plane

The edge of the inner region, i.e. where it connects to the outer region is the "matching plane". This edge is chosen so that the thickness of the gap at that location is still small enough that the lubrication assumption holds in the inner region but large enough that the outer mesh sufficiently resolves the flow in the outer region. During the course of the approach of the front to the particle this matching plane can change its location (i.e. along the ξ-direction) as well as width (i.e. along the η-direction). The "matching plane" location that is used in the current simulations corresponds to a d/R_{p} of 0.2, i.e. the gap thickness at that

location is comparable to the particle radius. The flowfields in the inner and outer regions need to be matched, i.e. information needs to be passed between the inner and outer regions so that the pressure and velocity fields are consistent at the boundary separating the two regions.

2.4.1. Boundary conditions for the "inner region" at the "matching plane"

The flow-fields in the inner and outer regions need to be matched at the matching plane as shown in Fig. 2. Since the equation in the inner region is a lubrication equation (where pressure is the independent variable to be solved), pressure boundary conditions are needed from the outer region. At the matching plane, the averaged outer region pressure values are supplied as the boundary conditions for the inner region pressure equation, Eq. (26). Note that since the pressure of the outer flow has a different scale than that of the inner flow, the pressure that is applied at the inner region must be expressed in the scale of the inner flow. Hence the dimensionless outer pressure must be multiplied by the scaling factor, $Z_f = p_{Couter}/p_{Cinner}$, in order to be used as the boundary condition for Eq. (26). The disjoining pressure is not included in the boundary condition as it is negligible at the matching plane.

2.4.2. Boundary conditions for the "outer region" at the "matching plane"

When the particle is in motion, there is a net mass flux of melt that is required to enter or leave the lubrication layer to replenish the melt in the inner region. Viewed from the outer region, the matching plane behaves as an outflow boundary. This outflow boundary is embedded inside the overall computational domain as opposed to residing at its edges. Nevertheless, standard outflow boundary conditions are applied at the matching plane while solving for the outer flow.

The matching between the flow in the inner region and that in the outer region is effected through the fact that the volume flux to be supplied at the matching plane is given by the rate of change of volume of the lubrication layer i.e.:

$$Q^* = \left(\frac{V_c}{U_c}\right)\int_0^{\xi^*_{max}} (v^*_p - v^*_{s\text{-}l})\,d\xi^* \tag{35}$$

Assuming a parabolic velocity profile at the matching plane (i.e. the inlet to the inner region and outlet to the outer region) the outflow velocity profile for the outer region at the matching flow is given by:

$$U^*_{match} = a_U\left(\frac{d_c}{R_p}\eta^*\right)^2 + b_U\left(\frac{d_c}{R_p}\eta^*\right) + c_U \tag{36}$$

where U^*_{match} is the fluid velocity in the ξ^*-direction located at the matching plane, and a_U, b_U, and c_U are determined from boundary conditions. The $\left(\frac{d_c}{R_p}\right)$ factor ensures that the "outer" scaling is used.

The following boundary conditions apply to this parabolic profile:

$$U^*_{match}(\eta^* = 0) = U^*_{s\text{-}l} = 0 \tag{37}$$

$$U^*_{match}(\eta^* = d^*) = U^*_p \tag{38}$$

The expression for the outflow velocity then is:

$$U^*_{match} = a_U\left(\frac{d_c}{R_p}\eta^*\right)^2 + \left(\frac{(U^*_p - U^*_{s\text{-}l}) - a_U\left(\frac{d_c}{R_p}d^*\right)^2}{\left(\frac{d_c}{R_p}d^*\right)}\right)\left(\frac{d_c}{R_p}\eta^*\right) + U^*_{s\text{-}l} \tag{39}$$

The constant a_U is obtained by matching the volume flux, Eq. (39), to that produced by the above parabolic inflow at the matching plane:

$$\left(\frac{d_c}{R_p}\right)\int_0^{d^*} U^*_{match}\,d\eta^* = Q^* \tag{40}$$

Substituting Eq. (39) into Eq. (40) and integrating results in an equation for the constant, a_U:

$$a_U = \frac{6\left(Q^* + U^*_{s\text{-}l}\left(\frac{d_c}{R_p}d^*\right)\right)}{\left(\frac{d_c}{R_p}d^*\right)^3} + \frac{3(U^*_p - U^*_{s\text{-}l})}{\left(\frac{d_c}{R_p}d^*\right)^2} \tag{41}$$

Substituting Eqs. (35) and (41) into Eq. (39) leads to a solution for U^*_{match} that is used for the boundary condition for the outer flow.

A pressure boundary condition for the "outer domain" is now required. To conform with the outflow boundary treatment for the matching plane a zero normal pressure gradient is applied for the outer flow. The normal to the matching plane is easily obtained using the level-set field in that region.

2.5. Temperature of the interfaces in the gap

The temperature of the solidification front is given by Eq. (5). To find the particle surface temperature heat flux balance (Eq. (6)) is applied at the particle–liquid interface.

The gradients in Eq. (6) are evaluated using a normal probe technique [28]. When the particle and front are far apart there are sufficient points available in the liquid and particle interior to use two probe points on the normal probe to extract gradients [28]. However, when the particle is approached by the front it is not possible to use the probe technique to estimate gradients in the liquid melt since the layer of melt between the particle and front can be very thin (i.e. below the resolution afforded by the mesh). To allow for this situation, only one point is used on the normal probe. Then the above gradients are discretized as:

$$k_p\left(\frac{T^*_{ps} - T^*_p}{\Delta n^*}\right) = k_l\left(\frac{T^*_p - T^*_{s\text{-}l}}{\frac{d_c}{R_p}d^*}\right) \tag{42}$$

where Δn^* is a probe that is placed normal to the particle surface and the temperature value at the end of the probe is interpolated from the surrounding mesh points. The T^*_{ps} is the temperature at the probe located inside the particle and the T^*_p is the temperature at the particle surface. Notice that the gap thickness is rescaled using the outer scale, R_p, this ensures the length-scales on each side of the equation are commensurate with each other.

Thus, when the front approaches the particle close enough that the lubrication model for the melt layer holds, the particle temperature can be found from:

$$T^*_p = \frac{T^*_{s\text{-}l} + \frac{k_p}{k_l}\left(\frac{\frac{d_c}{R_p}d^*}{\Delta n^*}\right)T^*_{ps}}{\left(1 + \frac{k_p}{k_l}\frac{\frac{d_c}{R_p}d^*}{\Delta n^*}\right)} \tag{43}$$

2.6. Computing solidification front velocity

The procedure to find the solidification front velocity in the outer region has been presented in previous papers [28]. A normal probe technique is used to compute the temperature gradients in the Stefan condition (Eq. (4)). In the inner region, computation of the temperature gradient in the liquid phase using the normal probe technique is not possible due to lack of sufficient mesh points across the gap. The method for calculating the temperature gradient in the liquid in the inner region is as follows:

From Eq. (18), the temperature in the gap assumes a linear profile. The boundary conditions are:

$$T^*(\eta^* = 0) = T^*_{s\text{-}l} \tag{44}$$

$$T^*(\eta^* = d^*) = T^*_p \tag{45}$$

Using these boundary conditions in Eq. (18) leads to a solution for the temperature equation in the gap:

$$T^* = \left(\frac{T^*_p - T^*_{s\text{-}l}}{d^*}\right)\eta^* + T^*_{s\text{-}l} \tag{46}$$

Taking the derivative of Eq. (46) with respect to $\frac{d_c}{R_p}\eta^*$ (the scaling factor ensures an "outer scale") leads to:

$$\frac{R_p}{d_c}\frac{\partial T^*}{\partial \eta^*} = \left(\frac{T^*_p - T^*_{s\text{-}l}}{\frac{d_c}{R_p}d^*}\right) = \left(\frac{\partial T^*}{\partial n^*}\right)_l \tag{47}$$

This provides the temperature gradient in the gap (liquid) that can be used in the Stefan condition (Eq. (4)) when finding the interface velocity. The temperature gradient in the solid, $\left(\frac{\partial T^*}{\partial n^*}\right)_s$, can be obtained by simply using the probe technique as in the outer domain calculation [19].

The linear temperature profile given in Eq. (18) suggests that all that is needed in order to obtain the solidification velocity from the Stefan condition (Eq. (4)) are the surface temperatures of the particle and the solidification front. The temperature field at the gap and matching plane is obtained from Eq. (18) as well.

2.7. Computing particle motion

Previous steady-state as well as dynamic analyses of particle–front interactions have employed analytical/empirical models for the forces experienced by the particle [4,5,7,9–12,14,15,33–35]. In the present work, the force acting on the particle is computed directly from the fluid mechanics in the inner and outer regions. Thus, once the pressure in the embedded lubrication model and the flow solution in the outer domain are obtained, the forces acting on the particle can be obtained as follows:

$$\sum \vec{F} = \vec{F}_{inner} + \vec{F}_{outer} \tag{48}$$

where

$$\vec{F}_{inner} = -(R_p p_{Cinner}) \int_A p^*_{inner}\vec{n}\,dS^*_{inner} \tag{49}$$

and

$$\vec{F}_{outer} = -(R_p p_{Couter}) \int_A p^*_{outer}\vec{n}\,dS^*_{outer} \tag{50}$$

where $\vec{F}_{inner}$ and $\vec{F}_{outer}$ are the (dimensional) forces in the inner and outer regions, respectively. The and dS^*_{outer} denotes the non-dimensional surfaces in the inner region and the outer region, respectively. The contribution to the forces from the shear component is assumed to be negligible compared to the large lubrication pressure force, and hence it is ignored in the calculation of the forces.

Once the forces are obtained, they can then be used to calculate the motion of the particle:

$$\frac{d\vec{v}^*_p}{dt^*} = \frac{t_c}{U_c m_p}(\vec{F}_{inner} + \vec{F}_{outer}) \tag{51}$$

The vector, $\vec{n}$, in Eqs. (49) and (50) is the normal to the particle surface in global x- and y-coordinates. Hence, the velocity vector in Eq. (51) is also in the global x- and y-coordinate system. The reason behind using the global coordinates is because the level-set advection of the interfaces requires the global coordinates. The velocities are transformed back in to ξ- and η-coordinates using Eqs. (9) and (10) whenever Eq. (26) is solved.

The gap thickness is then evolved according to:

$$\frac{dd^*}{dt^*} = \frac{V_c t_c}{d_c}(V^*_p - s^*_{s\text{-}l}) \tag{52}$$

where $s^*_{s\text{-}l}$ is the solidification velocity (as obtained by the Stefan condition, Eq. (4)) and V^*_p is the particle velocity in the η^* direction (both of which are in the normal direction of the solidification front). Note that all variables in Eq. (52) are functions of ξ^*.

2.8. Time-stepping of the inner and outer equations

An important issue that needs to be addressed in the coupling of the inner and outer solutions is the disparity in the physical time scales and hence the numerical time step choice. The time-step size of the outer region solution, including level-set advection, is determined by the

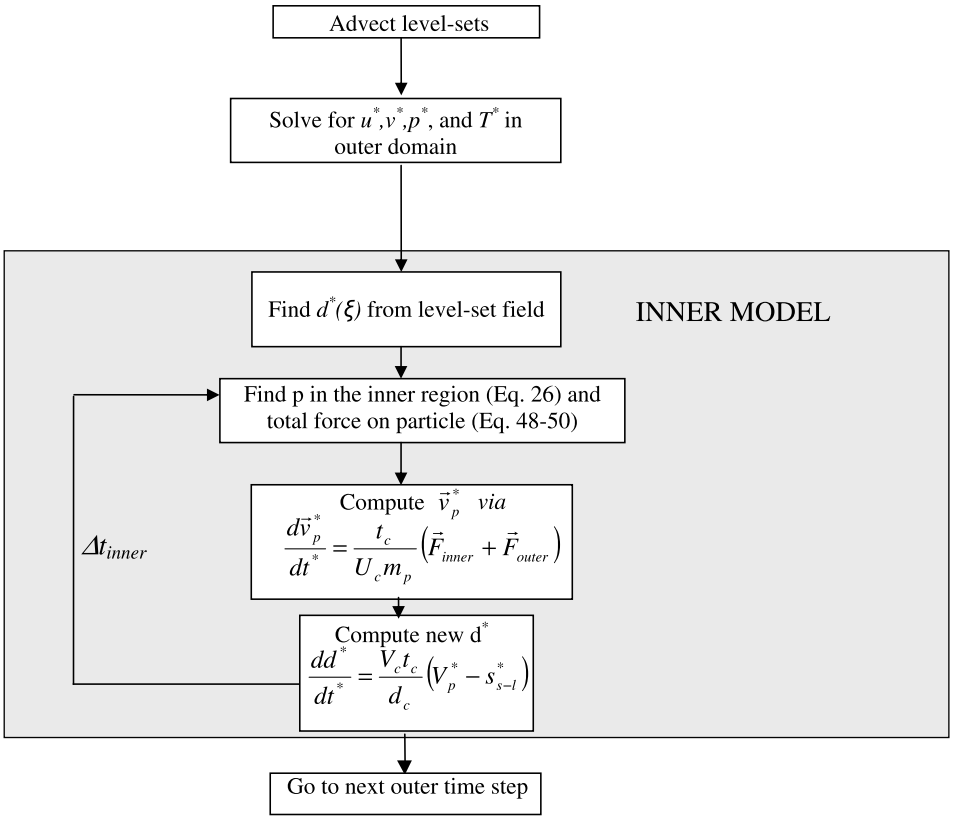

Fig. 4. Flowchart of the overall solution procedure.

solidification front velocity and the outer mesh size [18]. Since the inner region length scale (i.e. melt gap thickness) is typically very small, advecting the level-set at the outer time step size could cause the solidification front to collide with the particle. To circumvent this, once the solidification front approaches the particle to small separations, the outer time step size, Δt_{outer}, is restricted such that:

$$\Delta t_{\text{outer}} = \min\left(\left|S\frac{\left(\frac{d_c}{R_p}d^*\right)}{(V_p^* - s_{s\text{-}l}^*)}\right|, \quad \text{CFL}\frac{\Delta x^*}{\max(|V_p^*|, |s_{s\text{-}l}^*|)}\right) \tag{53}$$

The first argument in the brackets on the right hand side sets the time-step such that the solidification front will not collide with the particle, with S acting as a safety factor. The second argument in the brackets is the typical CFL-type condition where Δx^* is the outer grid size and CFL is the interface Courant–Friedrichs–Lewy constant.

To obtain stable results from the embedded lubrication model (i.e. Eqs. (26) and (48)–(52)), one has to choose time-steps commensurate with the inner time-scale. To ensure full coupling in time between the inner and outer region, solving the outer region equations at the inner time-scale would be ideal but is impractical because this would require an impossible number of time-steps to see any significant changes in the outer solution. To remedy this situation, the embedded lubrication model is advanced in time using an inner time-step size different from the outer region time step. To match solutions in time however the inner region equations are solved for a period of time equal to that of the micro time-step used for the outer domain solution. The inner and outer time-step sizes are related by:

$$\Delta t_{\text{inner}} = \frac{\Delta t_{\text{outer}}}{\tau} \tag{54}$$

where Δt_{inner} is the inner lubrication model time step, Δt_{outer} is the outer model time step. The parameter, τ, has to be defined such that Δt_{inner} becomes commensurate with the inner time scale and keeps the solution of the inner model stable. Typical minimum gap thicknesses ($d_{\min}$) are of the order of nanometers (10^{-9} m) and the outer lengthscale (R_p) is of the order of micrometers (10^{-6} m). Therefore $\tau = \frac{\Delta t_{\text{outer}}}{\Delta t_{\text{inner}}}$ is of the order of 1000 since $\Delta t_{\text{outer}} = \frac{R_p}{U_c}$ and $\Delta t_{\text{inner}} = \frac{d_{\min}}{U_c}$. In the present calculation, τ was set to 5000. The inner lubrication model is then evolved with this inner time step until the time elapsed in the inner model is equal to that of the outer time step. An illustration of the manner in which the inner and outer models are coupled is outlined in Fig. 4.

3. Results

3.1. Validation of the embedded lubrication model

The above methodology for coupling the outer and inner scales involves the following major computational aspects:

1. Accurate tracking of solid–liquid front evolution in the presence of diffusional heat transport.
2. Computation of fluid flow in the presence of moving solid boundaries (i.e. the particle and the phase boundary).
3. Solution of the lubrication equations and the computation of forces on the particle (outer region) due to the flow in the lubrication film (inner region).
4. Coupling of the flow and heat transfer in the outer region with that in the inner region.

The first two aspects have been thoroughly validated in previous work [18,19]. The third aspect, i.e. the solution of the lubrication layer equations in the presence of moving boundaries can be validated for the case of a cylinder moving with a velocity of $\vec{v}_p = -v_p\hat{j}$ (where $\hat{j}$ is the unit vector in the y-direction) downwards towards a stationary flat plate, as shown in Fig. 5. Note that this is strictly a validation of the fluid flow calculation in the gap and for the computation of the coupling of the inner and outer flow solutions; the temperature field and solidification front evolution are not involved in this case.

For the case of a cylinder moving toward a flat plate at constant speed v_p (Fig. 5a) and for low Reynolds numbers, an analytic expression for the pressure profile underneath the particle is given by Leal [32] as:

$$P(\xi) = -6\mu R_p v_p \left[\frac{1}{\left(d_{min} + \left(\frac{\xi^2}{2R_p}\right)\right)^2} - \frac{1}{\left(d_{min} + \left(\frac{\xi_{max}^2}{2R_p}\right)\right)^2} \right] \tag{55}$$

where $P(\xi)$ is the pressure field in the lubrication layer between the particle and the plate, ξ_{max} is the distance from the symmetry line ($\xi = 0$) to the edge of the lubrication layer. In the present paper this corresponds to the matching plane

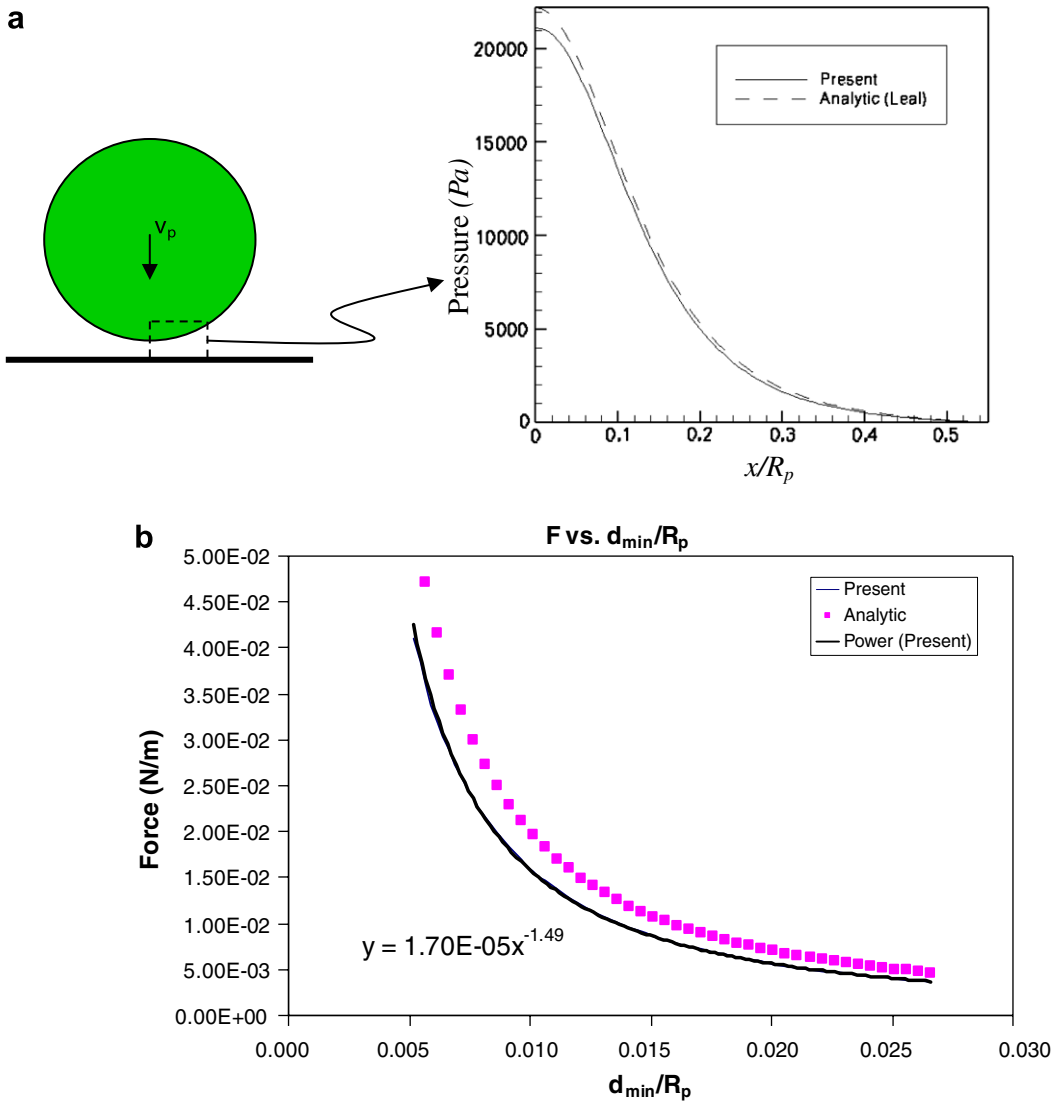

Fig. 5. (a) Pressure distribution in the gap for a 1 μm particle approaching a plane wall at 500 μ/s at $d_{min}/R_p = 0.02$ (no disjoining effects included). (b) The force as a function of d_{min}/R_p obtained from one simulation of a particle approaching a flat wall. The bold line represents a power law fit curve which lies directly above the actual data line.

identified in Section 2.4. d_{min} is the minimum gap thickness, i.e. the gap thickness at the symmetry line below the particle.

Computation of the flow in the inner and outer regions was performed for the configuration described above. Comparison of the numerical results with the analytical solution is shown in Fig. 5a and b. The pressure profile given by Eq. (55) is plotted in Fig. 5 for a $d_{min}/R_p = 0.020$, $R_p = 1\ \mu m$, $v_p = 500\ \mu/s$. With a viscosity of 0.003 Pa s the Reynolds number is 4×10^{-4}. The pressure profile obtained by solving a lubrication equation (Eq. (26)) in the inner region is also plotted in Fig. 5. As seen in Fig. 5, the calculated profile from the pressure Poisson equation (Eq. (26)) is in good agreement (to within a few percent) with the analytic expression obtained by Leal [32].

The total force on the particle during its steady-state motion towards the plate is [32]:

$$F_{D,ANAL} = -3\sqrt{2}\pi\mu v_p \left(\frac{R_p}{d_{min}}\right)^{1.5} \tag{56}$$

The force on the particle computed from the coupled inner/outer flow solution is plotted along with the analytic result in Fig. 5b. Notice that the curve fit to the computed force data yields:

$$F_D = -3.61\pi\mu v_p \left(\frac{R_p}{d_{min}}\right)^{1.49} \tag{57}$$

The computed force expression reproduces the correct power-law exponent and the overall trend with varying d_{min}/R_p (to within a few percent) when compared with the analytical result of Leal. The observed difference between the analytical and numerical curves is attributed to the fact that the gap thickness variation along ξ is obtained from the (outer) level-set field which contains errors due to interpolation and estimations of the distance function. The difference over the entire range of d/R_p, however, is small and the method is considered to be validated.

3.2. Simulation of solidification front–particle interactions

To perform numerical experiments under controlled conditions, a directional solidification process (with the solidification boundary moving up) is simulated. This configuration (Fig. 6) corresponds to that used in previous experimental [33,36] as well as theoretical [9,11–13,33] work on particle–front interactions. In the numerical model to simulate directional solidification, because the overall domain is stationary, the heater is translated rather than the sample. To simulate this condition, temperature boundary conditions at the top and bottom of the domain are varied in time to reflect this motion of the heaters. At the top of the domain the liquid is given a temperature:

$$T_L = T_{LO} - G_L v_s t \tag{58}$$

where T_{LO} is the initial temperature of the top boundary, G_L is the temperature gradient in the liquid, and v_s is the pull velocity (i.e. imposed solidification velocity) of the sample in directional solidification.

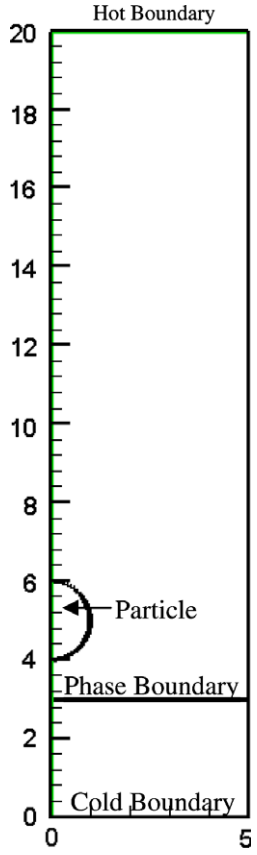

Fig. 6. Initial system setup.

At the bottom of the domain, i.e. on the solid side, the boundary condition is:

$$T_S = T_{SO} - G_S v_s t \tag{59}$$

where T_{SO} is the initial temperature of the bottom boundary and G_S is the imposed temperature gradient in the solid. Non-dimensionalizing using the outer scales, Eqs. (58) and (59) become, respectively:

$$T_L^* = T_{LO}^* - Pe_L t^* \tag{60}$$

$$T_S^* = T_{SO}^* - Pe_S t^* \tag{61}$$

where $Pe_L = v_s R_p/\alpha_l$ and $Pe_S = (G_S/G_L)(v_s R_p/\alpha_l)$ denote the liquid and solid Peclet number, respectively. The fluid velocities at the top and bottom faces of the computation domain are set to zero. Symmetry boundary conditions are applied on all variables at the left and right boundaries.

The particle is initially placed in the center of the computational domain and the solidification boundary is placed some distance below it, as shown in Fig. 6. To obtain suitable initial conditions, the system is first brought to steady-state by solving the heat conduction equation for an extended time before the phase boundary is allowed to move. After the steady-state temperature values are reached, the phase boundary is allowed to move towards the particle. Once the ratio of the minimum gap thickness

(d_{min}) to R_p reached a value of 0.15, the lubrication model is activated and the subsequent interaction is simulated using the coupled multiscale model.

A grid convergence study is first performed in order to choose an adequate grid size for the computations. Premelting effects on the interface temperature are not included in this case (i.e. $\lambda = 0$), the particle radius is 1 μm, and the solidification front velocity is 100 μm/s. The ratio of thermal conductivities $k_p/k_l = 1$. The values of other parameters used in these simulations correspond to typical MMCs [7,33,36] and are given in Table 1. Three grid sizes were employed in the calculations in the region occupied by the front and particle through the interaction.

Table 1
Values of the constants/material properties used in calculations (the values for the material properties were adopted from [9])

Constant/material properties	Definition	Value used in present calculations
μ	Dynamic viscosity of melt	0.003 Pa s
ρ	Density of melt	2365 kg/m^3
R_p	Particle radius	10^{-6} m
G_L	Temperature gradient in the melt	10^4 K
A	Hamaker constant	-8.0×10^{-19} J
λ	Interaction length used in premelting expression	2.0×10^{-10} m
k_l	Thermal conductivity of the melt	100 W/mK
k_s	Thermal conductivity of the solid	100 W/mK
k_p	Thermal conductivity of the particle	1–100 W/mK
α_l	Thermal diffusivity of the melt	5.15×10^{-5} m^2/s
T_m	Bulk melting temperature of the melt	933 K
H_{sl}	Latent heat of fusion per unit mass	399,000 J/kg

These are, respectively, ($\Delta x = \Delta y = 0.025$, 0.0325, and 0.04) in the region of $3.0 \leqslant y \leqslant 7.0$. The interaction between the front and the particle in this case results in steady pushing of the particle ahead of the front. Fig. 7 shows that the overall interaction is captured well on these grids with convergence of the particle velocity with increasing grid density. This is shown clearly in Fig. 7b with a magnified view of the final velocities assumed by the front–particle system.

Based on the above grid independence study, the grid size used in the simulations is a 202×322 grid, with a 202×160 grid points used in the region corresponding to $3.0 \leqslant y \leqslant 7.0$, i.e. where the particle and front were placed initially and where the subsequent interaction occured. The simulation presented as an example in this paper illustrates the various aspects of the calculation using the multiscale model, i.e. the outer region flow (Fig. 8), the matching flow between the outer and inner regions and the inner region geometry evolution (Fig. 9), inner region pressure profile (Fig. 10), and the overall evolution of the moving boundaries (Fig. 11). All conditions used are the same as for the grid independence study presented above except that the front velocity is increased to 500 μm/s.

3.2.1. Outer region

Fig. 8 illustrates the evolution of the temperature field, the outer region pressure and the streamlines as the solidification front and particle interact. Fig. 8a–c show the temperature fields for this case. The solidification front is indicated by the bold line corresponding to a temperature value of 933 K (which is the equilibrium melting temperature). Note that in this case the particle–front interaction led to a steady pushing mode, i.e. after a period of interaction, the particle was pushed steadily ahead of the front. The front remained planar through the interaction, even into the steady pushing regime. Fig. 8d–f show the pressure field and streamlines in the outer region at instants

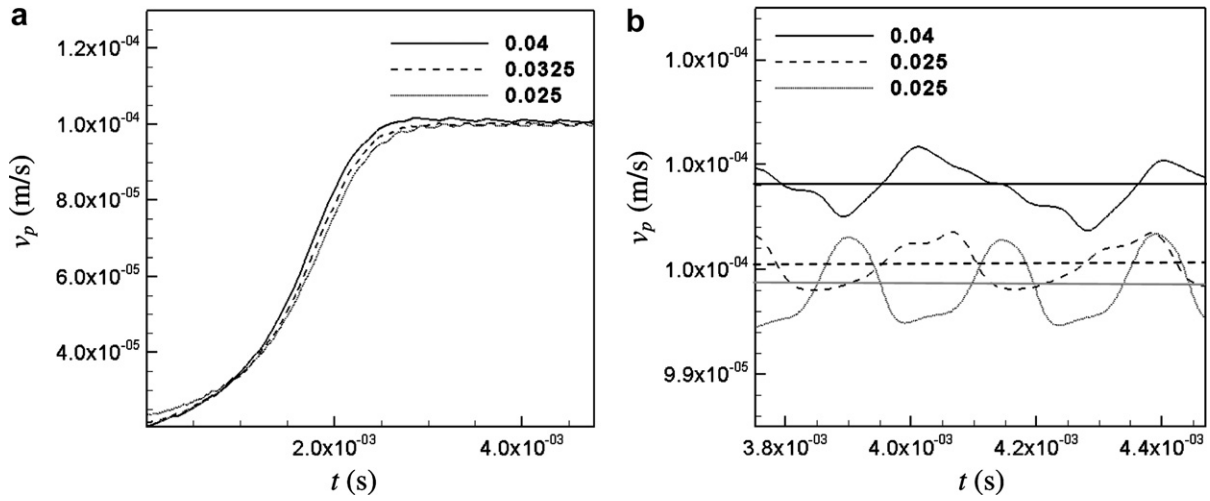

Fig. 7. Grid convergence study ($\Delta x = \Delta y = 0.025$, 0.0325, and 0.04) in the $y \in [3.0, 7.0]$ region. (a) Evolution of particle velocity with time. (b) Particle velocity vs. time at the culmination of the interaction when a "steady" pushing mode is reached in all three cases.

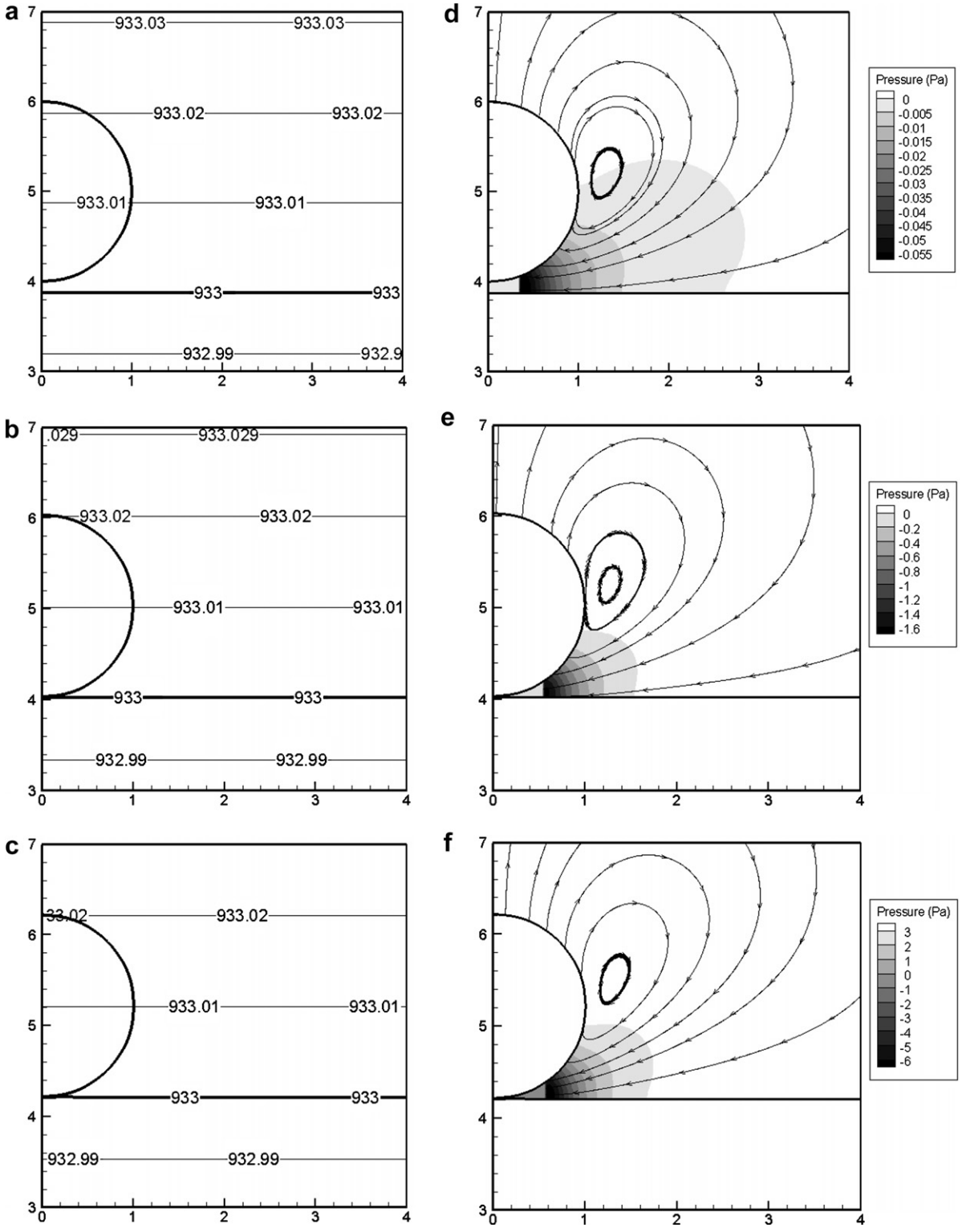

Fig. 8. Temperature contours (left) and the corresponding pressure contours and streamlines (right) of a system where the solidification velocity is 500 μm/s with no premelting, $k_p/k_l = 1.0$, and $R_p = 1$ μm. The axes are non-dimensional and are scaled by R_p. (a–c) The isotherms and interface location at three different (increasing) times. (d–f) The pressure field corresponding to the time instants in (a–c).

corresponding to Fig. 8a–c. Note that in each of these figures the pressure contours terminate at a certain point (i.e. at the matching plane) in the gap between the particle and the front. Since a steady pushing mode results from the interaction, the fluid flow from the outer region (Fig. 8f) is established to replenish the melt in the inner region as the front solidifies. To the left of the matching plane, i.e. where the outer region pressure contours are not shown,

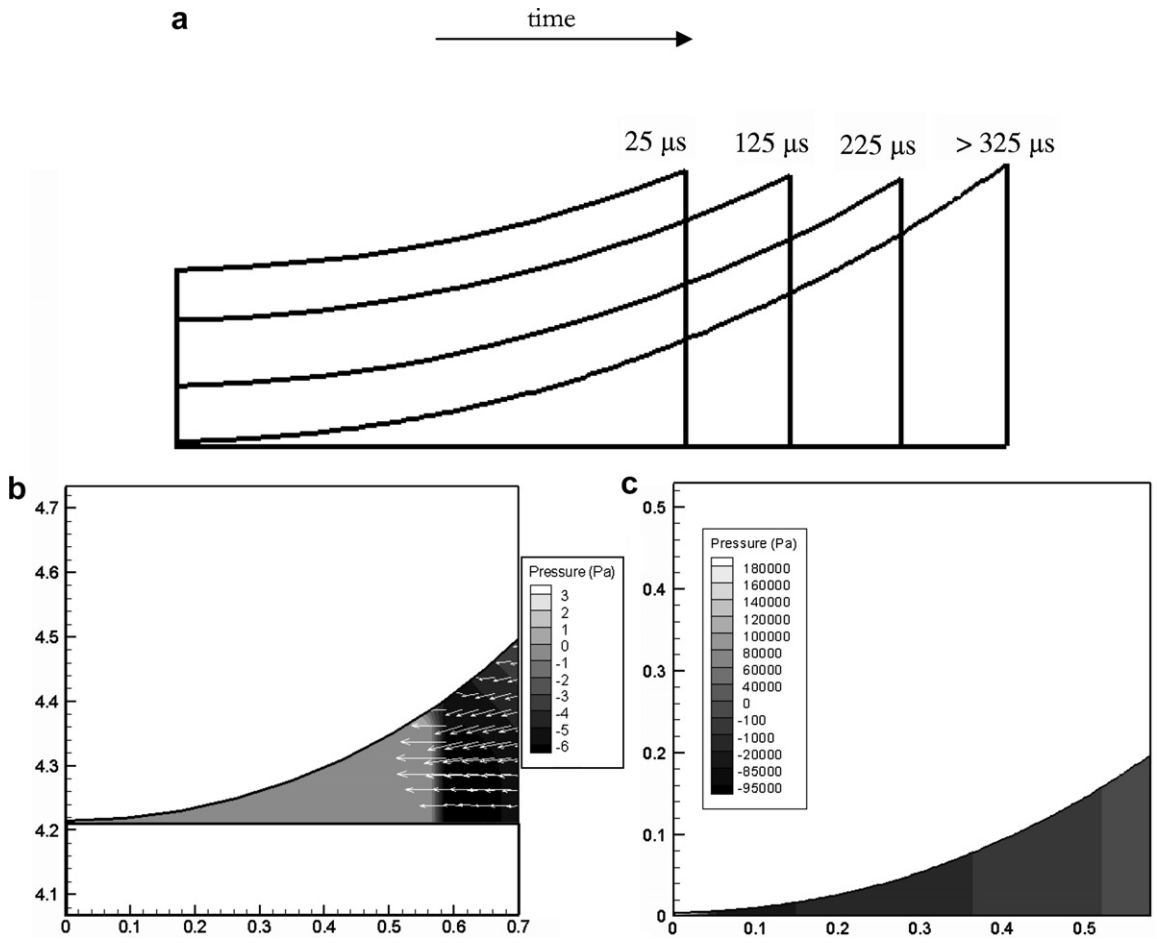

Fig. 9. Behavior of the interfaces and flow in the inner region for the case where solidification velocity is 500 μ/s, there is no premelting ($\lambda = 0$), $k_p/k_l = 1.0$, and $R_p = 1$ μm. (a) Evolution of the gap between the particle and the front. The front shape is shown at four different times. (b) Velocity boundary condition for the outer flow at the matching plane. (c) Inner gap pressure contour map at the steady pushing mode.

the outer flow calculations are replaced with the inner region lubrication flow solution.

3.2.2. Matching plane

Fig. 9 provides an illustration of the location of and boundary conditions at the matching plane (corresponding to the steady pushing state established in Fig. 8f). During the front–particle interaction the location of the matching plane changes as the inner region identified using the procedures described in Section 2.3.2 changes. Fig. 9a shows the evolution of the geometry of the inner region, i.e. the lubrication layer. Note that, for clarity, the gap shape is plotted relative to the position of the solidification front (the lower flat surface). As shown in the figure, the lateral extent of the gap increases with time, shifting the location of the matching plane to the right. Also, the minimum gap thickness characterized by d_{min} decreases with time until a steady-state is reached; the steady-state gap profile is shown at time of 325 μs. At the matching plane, Eq. (39) provides the outlet velocity profile that is used as the boundary condition for the outer region. This velocity profile (Fig. 9b) and the corresponding mass flux are obtained to replenish the melt in the inner region that is induced by particle motion (Eq. (51)). The pressure field calculated in the inner region using the lubrication equation, Eq. (26), is shown in Fig. 9c at the steady-state pushing condition corresponding to Fig. 8c and f. At the matching plane the outer pressure field is supplied as the boundary condition in computing the inner lubrication layer pressures using Eq. (26). As can be seen very large pressures are developed in the gap leading to forces that tend to push the particle ahead of the front.

3.2.3. Inner region

The evolution of the pressure in the inner region is shown in Fig. 10 for the time instants corresponding to Fig. 8. At the initial stage the gap thickness is large and the disjoining pressure forces are just beginning to make their repulsive effect felt. The pressure profile in Fig. 10a shows that there are hardly any negative values of pressure in the gap, i.e. the viscous losses in the lubrication layer are small at this time. At the right edge (i.e. the "matching plane") the pressure levels out to a value that is equal to that of the outer flow. At a later time, when the gap

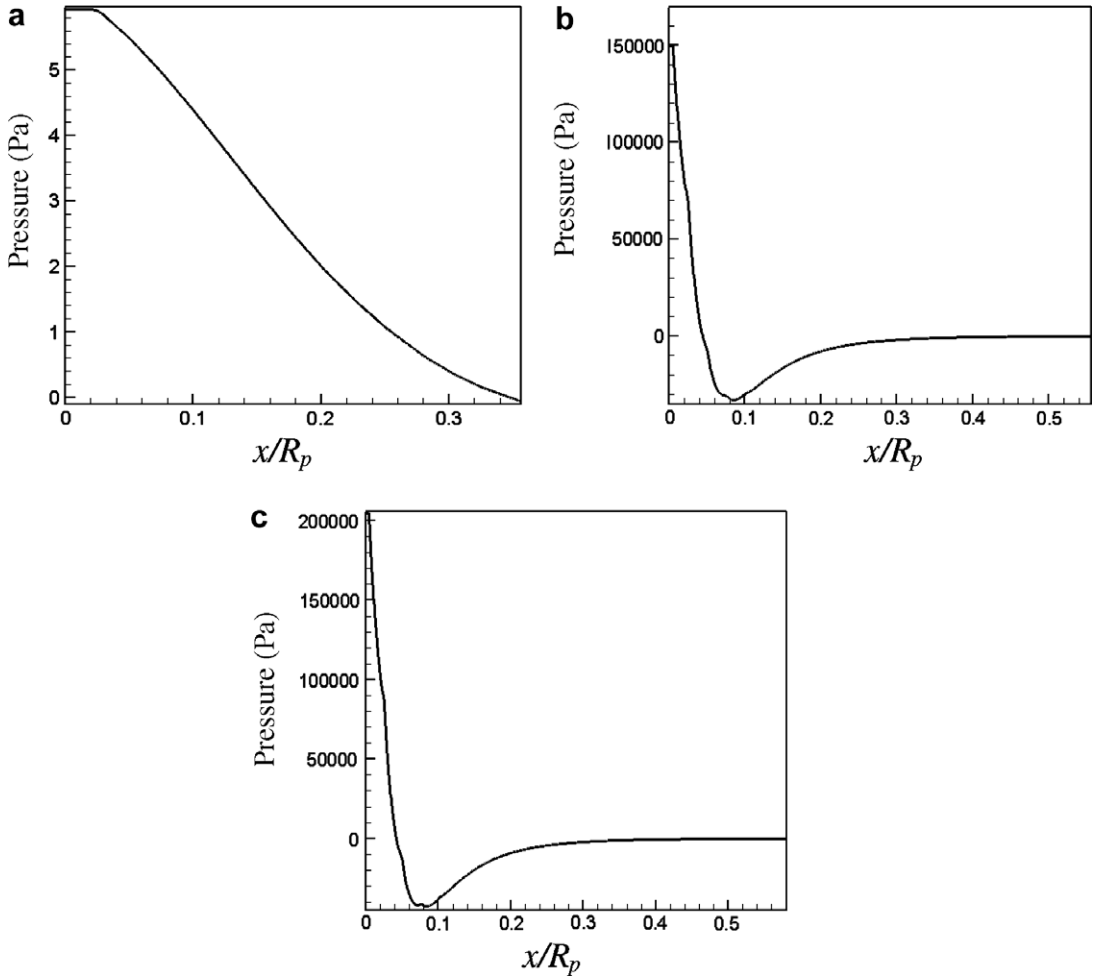

Fig. 10. Pressure profiles in the gap between the particle and the front as the system evolves to a final steady-state pushing mode. The profiles in (a–c) show the pressure in the gap at three different times during the evolution of the particle–front interaction. The solidification velocity is 500 μ/s, there is no premelting ($\lambda = 0$), $k_p/k_l = 1.0$, and $R_p = 1$ μm.

between the front and the particle has narrowed, the pressure obtains a large positive value on the left hand side of the curve due to the disjoining pressure effects in the gap. The disjoining pressures predominate over the pressure drop in the gap due to viscous losses (the classical lubrication effect), however, leading to the particle being steadily pushed ahead of the front. In the steady state pushing condition (Fig. 10c) the disjoining pressure that pushes the particle has settled to a very large positive (i.e. upward directed) value directly under the particle, where the gap is narrowest, while in the region between $x/R_p = 0.05$ and 0.2 the viscous losses in the gap suffered by the fluid coming in from the outer region predominate.

3.2.4. Overall dynamics of particle and front

The net effect of the coupled outer-inner dynamics on the evolution of the particle and the front is shown in Fig. 11. Fig. 11a shows plots of particle velocity (v_p) and solidification front velocity directly below the particle (v_t) and far away from the front (pull velocity v_s) against time. As seen from the figure the particle is initially stationary but is set in motion by the disjoining pressure forces when approached sufficiently closely by the front and is later pushed at a velocity equal to that of the front, i.e. a steady pushing mode results. Fig. 11b shows the evolution with time of the minimum gap thickness, i.e. the thickness of the gap directly beneath the particle on the symmetry line, plotted against time. As seen in the figure the gap thickness decreases steadily in time and reaches a fixed value at steady-state pushing. At steady-state pushing the gap thickness (5 nm) is much smaller than the particle radius (1 μm). Fig. 11c shows the forces that act on the particle during the interaction as they vary in time. The drag and repulsive forces are initially very small as the front is still some distance from the particle. In time, however, the forces rise steeply (the force $\propto d^{-3}$) and the balance between the repulsive disjoining pressure forces and the opposing drag forces is very delicate. This is shown in Fig. 11d where the total force acting on the particle is shown. Clearly, the difference between the opposing forces is small. It is also observed that the final steady-state pushing mode actually shows a slight oscillatory tendency.

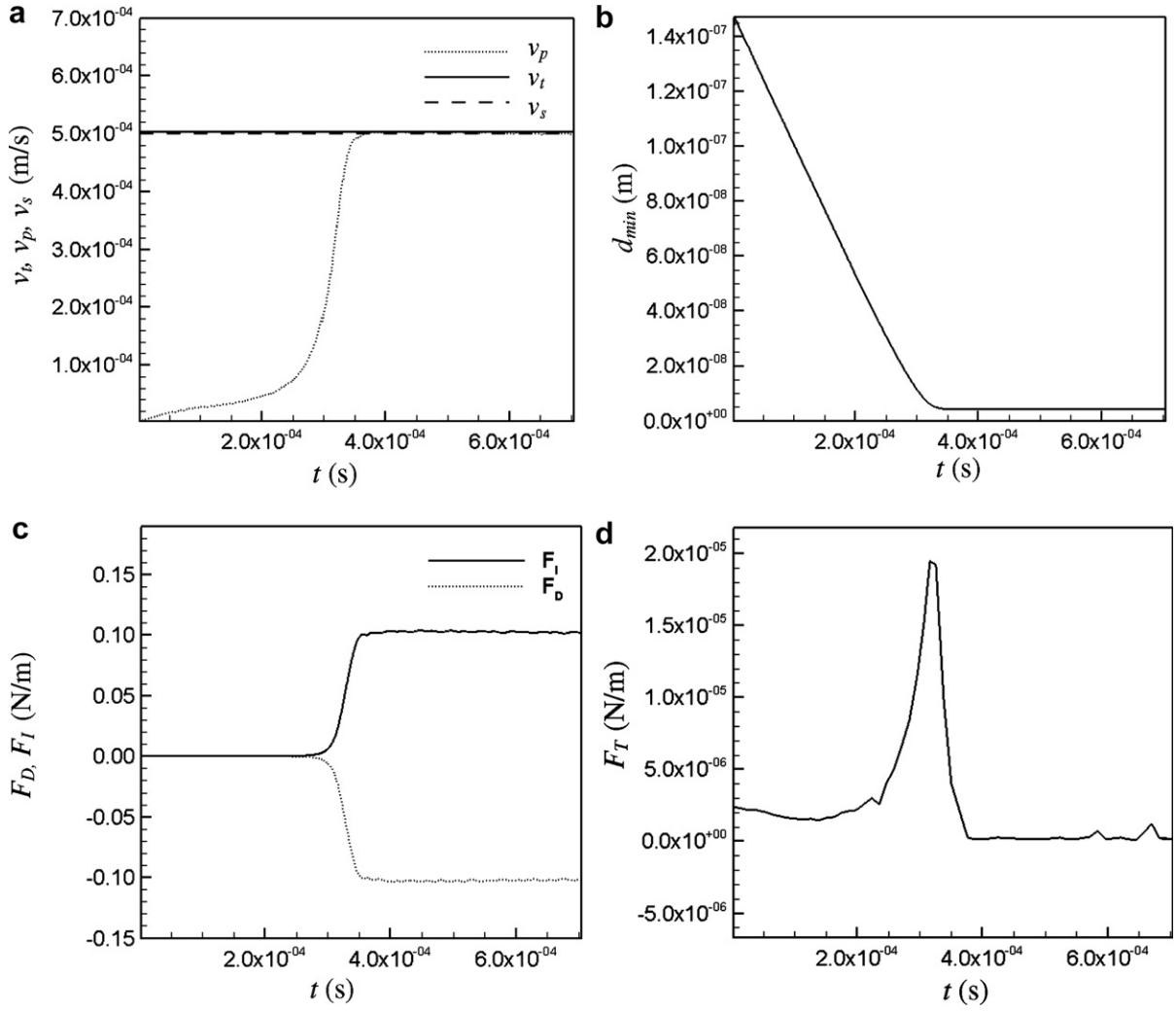

Fig. 11. (a) Velocity vs. time plot and (b) $d_{\min}$ vs. time plot. (c) Repulsive and drag force. (d) Total force on the particle. The solidification velocity = 500 μ/s, $\lambda = 0$ (no premelting effect), $k_p/k_l = 1.0$, $R_p = 1$ μm.

4. Conclusions

A multiscale approach is developed to study the interaction between an advancing solidification front and a particle embedded in the melt. The interfaces in the problem are tracked using a level-set approach and a previously developed Cartesian grid-based sharp interface method is used to solve the governing equations in the presence of the moving embedded interfaces. The computational domain is partitioned into two sub-domains, an outer region corresponding to the overall particle–front system and an inner region corresponding to the narrow gap between the front and the particle. The dynamics of the fluid, phase boundary and particle in this inner region has a crucial impact on the front–particle interaction dynamics. In the inner region, the flow and temperature fields, are solved using a lubrication model which includes the disjoining pressure and premelted layer effects. The solution of the lubrication model in the inner region is coupled to the solution of the flow in the outer region. The model computes the forces acting on the particle and moves the particle accordingly. The numerical method underlying the solution of the equations in the outer region has been thoroughly validated in previous work. The fluid flow solution in the lubrication layer and its coupling with the outer flowfield was validated for the case of a particle approaching a stationary flat plate for which an analytical solution exists. Results for particle–solidification interactions using this method are provided in the companion paper.

Acknowledgement

This work was supported by a NSF-CAREER award (CTS-0092750) to the third author.

References

[1] J.W. Garvin, H.S. Udaykumar, Drag on a particle being pushed by a solidification front and its dependence on thermal conductivities, J. Cryst. Growth 267 (3-4) (2004) 724–737.

[2] R. Asthana, S.N. Tewari, Second phase particle–solidification front interactions: an evaluation of theoretical models, Process. Adv. Mater. 3 (1993) 63–180.

[3] R. Asthana, S.N. Tewari, Review the engulfment of foreign particles by a freezing interface, J. Mater. Sci. 28 (1993) 5414–5425.
[4] G.F. Bolling, J. Cisse, A theory for the interaction of particles with a solidifying front, J. Cryst. Growth 10 (1971) 56–66.
[5] A.A. Chernov, D.E. Temkin, A.M. Mel'nikova, Theory of the capture of solid inclusions during the growth of crystals from the melt, Sov. Phys. Crystallogr. 21 (4) (1976) 369–373.
[6] A.A. Chernov, D.E. Temkin, A.M. Mel'nikova, The influence of the thermal conductivity of a macroparticle on its capture by a crystal growing from a melt, Sov. Phys. Crystallogr. 22 (6) (1977) 656–658.
[7] D.K. Shangguan, S. Ahuja, D.M. Stefanescu, An analytical model for the interaction between an insoluble particle and an advancing solid/liquid interface, Metall. Mater. Trans. A 23A (1992) 669–680.
[8] A.W. Rempel, M.G. Worster, The interaction between a particle and an advancing solidification front, J. Cryst. Growth 205 (1999) 427–440.
[9] A.V. Catalina, S. Mukherjee, D.M. Stefanescu, A dynamic model for the interaction between a solid particle and an advancing solid/liquid interface, Metall. Mater. Trans. A 31A (2000) 2559–2568.
[10] L. Hadji, Thermal force induced by the presence of a particle near a solidifying interface, Phys. Rev. E 64 (51) (2001) 51502/1–51502/6.
[11] J.W. Garvin, H.S. Udaykumar, Particle–solidification front dynamics using a fully coupled approach, Part I: Methodology, J. Cryst. Growth 252 (2003) 451–466.
[12] J.W. Garvin, H.S. Udaykumar, Particle–solidification front dynamics using a fully coupled approach, Part II: Comparison of drag expressions, J. Cryst. Growth 252 (2003) 467–479.
[13] J.W. Garvin, H.S. Udaykumar, Effect of a premelted film on the dynamics of particle–solidification front interactions, J. Cryst. Growth 290 (2) (2006) 602–614.
[14] D.R. Uhlmann, B. Chalmers, K.A. Jackson, Interaction between particles and a solid–liquid interface, J. Appl. Phys. 35 (1964) 2986–2993.
[15] A. Borsik, K.K. Kelemen, G. Kaptay, A dynamic model of ceramic particle–solidification front interaction, Mater. Sci. Forum 414–415 (2003) 371–376.
[16] J.N. Israelachvili, Intermolecular and Surface Forces, second ed., Academic Press, 1991.
[17] S.N. Omenyi, A.W. Neumann, Thermodynamic aspects of particle engulfment by solidifying melts, J. Appl. Phys. 47 (9) (1976) 3956–3962.
[18] S. Marella et al., Sharp interface Cartesian grid method I: an easily implemented technique for 3D moving boundary computations, J. Comput. Phys. 210 (1) (2005) 1–31.
[19] Y. Yang, H.S. Udaykumar, Sharp interface Cartesian grid method III: solidification of pure materials and binary solutions, J. Comput. Phys. 210 (1) (2005) 55–74.
[20] J.A. Sethian, Evolution, implementation, and application of level set and fast marching methods for advancing fronts, J. Comput. Phys. 169 (2) (2001) 503–555.
[21] J.A. Sethian, A. Vladimirsky, Ordered upwind methods for static Hamilton–Jacobi equations, Proc. Natl. Acad. Sci. USA 98 (20) (2001) 11069–11074.
[22] S. Osher, J.A. Sethian, Fronts propagating with curvature-dependent speed – algorithms based on Hamilton–Jacobi formulations, J. Comput. Phys. 79 (1) (1988) 12–49.
[23] J.A. Sethian, P. Smereka, Level set methods for fluid interfaces, Ann. Rev. Fluid Mech. 35 (2003) 341–372.
[24] G. Son, N. Hur, A level set formulation for incompressible two-phase flows on nonorthogonal grids, Numer. Heat Transf. Part B: Fund. 47 (5) (2005) 303–316.
[25] L.-L. Zheng, H. Zhang, An adaptive level set method for moving-boundary problems: Application to droplet spreading and solidification, Numer. Heat Transf. Part B: Fund. 37 (1–4) (2000) 437–454.
[26] H. Liu et al., Sharp interface Cartesian grid method II: a technique for simulating droplet interactions with surfaces of arbitrary shape, J. Comput. Phys. 210 (1) (2005) 32–54.
[27] J.G. Dash, H. Fu, J.S. Wettlaufer, The premelting of ice and its environmental consequences, Rep. Prof. Phys. 58 (1995) 115–167.
[28] Y. Yang, J.W. Garvin, H.S. Udaykumar, Sharp interface simulation of interaction of a growing dendrite with a stationary solid particle, Int. J. Heat Mass Transf. 48 (25-26) (2005) 5270–5283.
[29] A. Oron, S.H. Davis, S.G. Bankoff, Long-scale evolution of thin liquid films, Rev. Modern Phys. 69 (3) (1997) 931.
[30] W. Shyy et al., Computational Fluid Dynamics with Moving Boundaries, Taylor-Francis, Washington, DC, 1996.
[31] J.F. Thompson, Z.U.A. Warsi, C.W. Mastin, Numerical Grid Generation: Foundation and Applications, Elsevier Science Pub. Co., North-Holland, New York, 1985.
[32] G.L. Leal, Laminar Flow and Convective Transport Processes: Scaling Principles and Asymptotic Analysis, Butterworth, Boston, 1992.
[33] D.M. Stefanescu et al., Particle engulfment and pushing by solidifying interfaces: Part II. Microgravity experiments and theoretical analysis, Metall. Mater. Trans. A 29A (1998) 1697–1706.
[34] A.M. Zubko, V.G. Lobanov, V.V. Nikonova, Reaction of foreign particles with a crystallization front, Sov. Phys. Crystallogr. 18 (2) (1973) 239–241.
[35] R. Sasikumar, T.R. Ramamohan, Distortion of the temperature and solute concentration fields due to the presence of particles at the solidification front-effects on particle pushing, Acta. Metal. Mater. 39 (4) (1991) 517–522.
[36] F.R. Juretzko et al., Particle engulfment and pushing by solidifying interfaces: Part I: ground experiments, Metall. Mater. Trans. A 29A (1998) 1691–1696.